Urban-Target Recognition by Means of Repeated Spaceborne SAR Images

Daniele Perissin and Alessandro Ferretti

Abstract—The relative low resolution ($\sim$25 m $\times$ 5 m on the ground) of spaceborne C-band synthetic aperture radar (SAR) data as acquired, for example, by European Space Agency sensors ERS and Envisat, can be significantly increased (up to submeter precisions) by processing coherently long series of images. Moreover, by analyzing the amplitude of the radar signal and by exploiting polarization diversity, the main radar characteristics of urban targets can be estimated, and a system for automatic recognition of a set of scattering structures can be developed. In this paper, we study the variation of the amplitude of the received radar signal as a function of the acquisition geometry [normal baseline and Doppler centroid (DC)] to retrieve the extension of the targets in range and azimuth. The dependence of the radar amplitude on temperature at the time of acquisition has been discovered to be very useful to identify extended resonating targets. Dihedrals are discriminated from specular or trihedral reflectors through the phase of Envisat alternating polarization (AP) acquisitions. By means of all gathered radar measurements, the bases for the development of a system for the automatic recognition of six main typologies of urban SAR targets (ground-level and elevated backscatterers, simple and resonating dihedrals, poles and trihedrals) have been laid. Radar data are then combined with *in situ* surveys and aerial photos, allowing a first assessment of the methodology in urban area.

Index Terms—Interferometry, polarimetry, radar target recognition, synthetic aperture radar (SAR), urban areas.

I. INTRODUCTION

IN THE permanent scatterer (PS) technique, developed in the late 1990s at Politecnico di Milano [1]–[3], the coherent radar reflectors of a certain area of interest are exploited for overcoming the difficulties related to conventional synthetic aperture radar (SAR) interferometry (namely, phase decorrelation and atmospheric effects), achieving millimeter accuracy in monitoring relative displacements of the targets. Even if the PS technique has been an operational tool since 2000, the physical nature of the targets is still a subject of investigation. A good knowledge of the PS physical nature is a key step for a correct interpretation of the measured deformation mechanism. As an example, the phase of a dihedral formed by the ground and a building wall does not change in the presence of a building's slow subsidence, but it changes in case of ground subsidence [4]. In the second instance, the classification of reflecting structures behaving as PS allows an *a priori* identification of the PSs looking at the structural details of the buildings. Finally, knowing the PS's physical nature allows foreseeing their elec-

tromagnetic behavior under different acquisition geometries, frequencies, and polarizations, and feasibility studies on the integration of interferometric SAR multiple sensors can be developed [5], [6].

Up to now, the characterization and recognition of single radar targets have been tackled only by means of airborne high-resolution SAR images in urban sites [7]. Examples of high-resolution airborne SAR sensors are AER-II (FGAN) [8], ESAR (DLR) [9], RAMSES (ONERA) [10], PAMIR (FGAN) [11], mounting radars operating in different frequency bands (X, C, S, L, and P). Mainly exploiting X-band, techniques have been developed, e.g., for analyzing the different scattering mechanisms [12], for distinguishing superimposed scattering centers with polarimetric interferometric SAR data [13], and for evaluating the dependence of urban mapping on aspect and elevation angle [14]. These studies were applied, for example, to building reconstruction [15], damage detection [16], and grouping of regular point structures [17]. Building heights have been extracted through high-resolution SAR interferometry with different methodologies: shape from shadow [18], machine vision [19], stochastic geometry [20], and segmentation-based algorithms [21], [22]. Building characterization has been obtained using L-band polarimetric and interferometric SAR data [23]. Target detection has been achieved by developing despeckle filters [24], [25], jointly using radar image magnitude and phase [26], optimizing the radiometric estimation with spatial whitening filters [27]. Spatial distributed targets have been detected by filtering polarimetric channels [28]; sublook correlations have been proposed for ship detection [29]. Recently, orientation and dielectric properties of individual coherent targets have been extracted from their polarimetric and interferometric characteristics [30].

For what concerns target characterization, low-resolution spaceborne SAR data (as acquired, for example, by ERS) have been used up to now only for analyzing radiometric image properties even in urban areas. Usually, the imaged scene is partitioned in different terrain classes exploiting empirical statistical models [31] of the backscatter characteristic of materials. Details on the single building are not expected to be visible in spaceborne SAR data as long as new-generation high-resolution SAR systems are not operational (such as COSMO/SkyMed [32] or TerraSAR-X [33]). Therefore, the analysis is restricted to, for example, building-density estimates [34] or street recognition [35]. As a further step, in [36], more acquisitions at different times and view angles are shown, improving the characterization of urban areas. Only in the last years, as the European Space Agency (ESA) launched the new Envisat satellite, which provides simultaneous dual-polarization capability,

attempts of investigating urban targets in C-band have been made. Many works have been carried out on the combination of ERS and Envisat data [5], [37]–[44], and in [45] and [46], the polarization capability of Envisat has been exploited for discerning the scattering mechanism of urban coherent targets.

In this paper, the first actual characterization of PSs in C-band in urban areas by means of the ERS and Envisat data is shown. The most common urban-target typologies (gratings, roofs, poles, dihedrals, and trihedrals) have been identified, and an algorithm for radar automatic recognition has been developed. The results of the classification have been checked by means of aerial photography and *in situ* surveys—thanks to the submetric accuracy of target ground positioning of the applied technique.

The paper is divided into two main parts. In Section II, we analyze the theoretical basis and the processing chain that we developed; Section III reports the results obtained in the urban test site of Milan. Section II-A describes in more detail the general structure of the work, and the following sections analyze in-depth each single step: Section II-B—The complex SAR data are modeled as a function of a set of target parameters; Section II-C—The problem is inverted, searching for the target parameters; Section II-D—Based on the detected parameters, target classification is implemented. Finally, Section III shows a statistic of target parameters estimated from real data, together with the results of the classification (Section III-A), and describes the target typologies we identified through some meaningful examples (Section III-B), thus bringing experimental proofs of the reliability of the proposed technique.

II. THEORETICAL FRAMEWORK

A. General Formulation

The basic idea that underlies this paper is that, by exploiting many radar images acquired at different times with frequency, look angle, and polarization diversity, system resolution can be increased, and information on the physical nature of the targets can be achieved. Apart from a precise estimation of the 3-D position of the scatterer, the final goal of this paper is the identification of its typology. Such objective is obtained in two steps: 1) the estimate of a set of the target characteristics (feature extraction) and 2) the assignment of a class to the target based on the measured characteristics (labeling). The first step is a classical inverse problem [47], whose complexity is mainly due to the physical modeling of the acquisition process. The second step can be implemented through a general classification method. Again, here, the difficulty consists not in the classification procedure but in the determination of the target classes that can be separated using the data set under study.

The problem can be formalized as follows. Given N_I complex images $s_{i,k}$, with $i = 1, \ldots, N_I$ of the same target k, we search for the target typology $\mathcal{X}_k$. First, we need to identify the mutually independent degrees of freedom of the data set (as, e.g., acquisition time and geometry), which are identified by the vector $\mathbf{\Omega}$ of length N_Ω. Given the degrees of freedom, we expect to measure a set of the target characteristics (as, e.g., dimensions and orientation) included in the vector $\mathbf{\Theta}$

of length N_Θ. The complex radar signal $s_{i,k}$, relative to image i and target k, can then be expressed as

$$s_{i,k} = f(\mathbf{\Omega}_i, \mathbf{\Theta}_k) \tag{2.1}$$

where f is a function (generally not linear) that maps the parameter space $\mathbf{\Theta}$ into the data space s through the model space $\mathbf{\Omega}$. The first step of our algorithm consists in the problem-inversion searching for the target characteristics $\hat{\mathbf{\Theta}}_k$ that best fit the data s_k. Defining a specific norm $\|\|$, the solution is given by

$$\hat{\mathbf{\Theta}}_k = \arg\min_{\mathbf{\Theta}_k} \left(\sum_{i=1}^{N_I} \| s_{i,k} - f(\mathbf{\Omega}_i, \mathbf{\Theta}_k) \| \right). \tag{2.2}$$

Since the radar signal is complex, the dimension of the data space is $2N_I$. Thus, it is advisable that N_Θ be $\ll 2N_I$. In any case, the goodness of fit can be quantified by evaluating the residual ξ_k between data and model

$$\xi_k = \sum_{i=1}^{N_I} \left\| s_{i,k} - f(\mathbf{\Omega}_i, \hat{\mathbf{\Theta}}_k) \right\|. \tag{2.3}$$

The problem is optimized when each degree of freedom is exploited for resolving at least a target parameter: $N_\Theta \geq 2N_\Omega$.

Once we get the estimate of the characteristic vector $\hat{\mathbf{\Theta}}_k$, the target typology $\mathcal{X}_k$ is the output of the classification procedure $g: \mathbf{\Theta} \to \mathcal{X}$. The distance in the $N_\Theta - D$ space between the estimated class $\mathcal{X}_k$ and the point identified by $\hat{\mathbf{\Theta}}_k$ is the reliability of the classification result. In the following, we analyze in detail the physical aspects of the problem.

B. Forward Modeling

As already mentioned in the previous sections, the core purpose of this paper is to find a set of features that allows the recognition of the target typology by means of spaceborne SAR data in C-band. The problem is strictly dependent on the degrees of freedom of the available data set. In general, the wider the diversity of the illumination signal (e.g., more frequencies, view angles, polarizations, etc.), the larger the amount of information that can be extracted about the target. In this analysis, we consider a data set of N_I images acquired by the ESA sensors ERS and Envisat. In particular, we take advantage of the polarization capabilities of Envisat by exploiting also VV–HH alternating polarization (AP) acquisitions.

Thus, we identified the degrees of freedom of the problem in the variation of the following acquisition parameters with respect to a reference image (hereafter called Master):

1) interferometric normal baseline;
2) DC frequency;
3) central frequency (different between ERS and Envisat);
4) polarization;
5) time;
6) local temperature at the acquisition time.

The first two parameters are related to the acquisition geometry. Frequency and polarization characterize the illumination radiation, while the time of the acquisition and the local
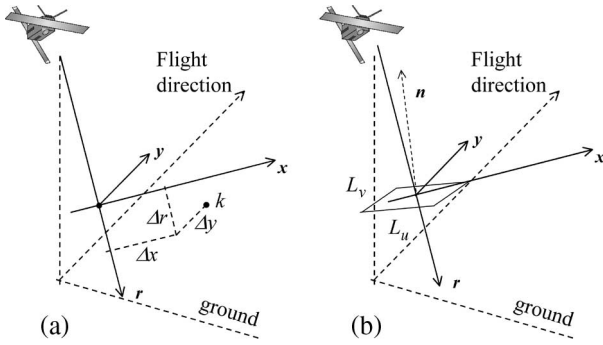
Fig. 1. Radar acquisition geometry of Master image. r-axis: slant range direction; y-axis: flight direction (azimuth); x-axis: normal to the ry plane (cross-slant range direction). (a) Point-wise target k with coordinates $\Delta r, \Delta x, \Delta y$. (b) Extended target lying in the origin of the Cartesian tern. The target is modeled as a planar surface of extensions $L_u \times L_v$ oriented as vector n.

temperature can be exploited successfully to extract further feature parameters useful for classification.

More precisely, we define the following reference system, as shown in Fig. 1:

1) r-axis: slant range direction of the Master image;
2) y-axis: flight direction (azimuth) of the Master image;
3) x-axis: normal to the ry plane (cross-slant range direction).

The Master sensor (index $i = 0$) illuminates the target with an incidence angle θ_0 ($\theta_0 \simeq 23°$ for ERS) and DC frequency f_{DC0}. Since the variations of the look angle are usually small for multitemporal data acquired along the same nominal orbit, the normal baseline $B_{n,i}$ of image i is proportional to a cross-track angle $\Delta\theta_i$

$$\Delta\theta_i = \frac{B_{n,i}}{R_0} \qquad (2.4)$$

where R_0 is the sensor-to-target distance for the Master acquisition ($R_0 \simeq 840$ km for ERS). Moreover, the DC frequency difference $\Delta f_{DC,i}$ of image i can be easily related to squint angle variations $\Delta\psi_i$ [5], [48]

$$\Delta\psi_i = \frac{\lambda_i}{2\delta_{az}\text{PRF}}\Delta f_{DC,i} \qquad (2.5)$$

where λ_i is the wavelength, δ_{az} is the azimuth sampling interval, and PRF is the pulse repetition frequency.

Within the analyzed data set, N_I' images are acquired at frequency $f_i = f_0$, and N_I'' images are obtained at frequency $f_i = f_0 - \Delta f$, where $\Delta f = 31$ MHz is the frequency gap between the ERS and Envisat sensors. Considering the ith image, we call t_i [days] its temporal baseline with respect to the Master image and T_i [°C] the temperature at its acquisition time (again referred to the Master one). As long as the polarization is concerned, since we suppose to use only Envisat VV–HH AP acquisitions, we introduce the variable η_i to indicate if the ith image has been acquired with VV pol ($\eta_i = 0$) or HH pol ($\eta_i = 1$).

Thus, the vector characterizing the degrees of freedom of an image of the data set is defined as follows:

$$\mathbf{\Omega} = [B_n, f_{DC}, f, T, t, \eta]. \qquad (2.6)$$

1) Phase Analysis: We look now for the target characteristics that can be observed under the variation of the previously described acquisition parameters. For the sake of simplicity, we will start our analysis by considering a pointwise target, i.e., an object much smaller than the resolution cell (about 20 m × 5 m on the ground for ERS). The target k has coordinates Δr_k, Δx_k, and Δy_k in the reference system shown in Fig. 1(a). In general, the target will be modeled under the first-order Born approximation as the sum of a high number of elementary point targets with no mutual interaction on an absorbing background.

The pixel complex value[1] of the ith image $s_{i,k}$ in correspondence of target k can be approximated as the sum of elementary reflectivities along the range direction

$$s_{i,k} \simeq \int \sigma_k e^{-j\frac{4\pi}{c}f_i r_{i,k}} dr \qquad (2.7)$$

where $r_{i,k}$ is the distance between the elementary reflectivities and the sensor. If the target is pointwise, the pixel complex value becomes

$$s_{i,k} \simeq \sigma_k e^{-j\phi_{i,k}} \qquad (2.8)$$

where $\phi_{i,k} = (4\pi/c)f_i r_{i,k}$. Assuming that all images have the same origin of the slant range axes, as in Fig. 2(a) and (b), the pixel phase can be rewritten, highlighting its variation with respect to the Master acquisition (the interferometric phase) $\phi_{i,k} = \phi_{0,k} + \Delta\phi_{i,k}$.

As derived in [5], the interferometric phase that depends on the acquisition geometry can be written as a function of the normal baseline $B_{n,i}$ and of the differences of central and DC frequencies Δf_i and $\Delta f_{DC,i}$, respectively, with respect to the Master one (c is the speed of light)

$$\Delta\phi_{i,k}^{geo} = -\frac{4\pi}{c}\Delta f_i \Delta r_k + \frac{4\pi f_i B_{n,i}}{cR_0}\Delta x_k + 2\pi\frac{\Delta f_{DC,i}}{\text{PRF}}\frac{\delta y_k}{\delta_{az}}. \qquad (2.9)$$

From (2.9), it is evident to recognize the dependence of the interferometric phase on the 3-D location of the target (δy_k is its azimuth subpixel position). Thus, in general (when different normal baselines and DC and carrier frequencies are present), the interferometric phase can be exploited for deriving the precise target 3-D coordinates, as already discussed in [49].

Assuming that the target k is affected by a motion (slow in comparison with wavelength and repeat cycle), the interferometric phase changes accordingly. We take into account two main motion components: a trend linear with time [1] and a seasonal component [3], [49] proportional to the temperature at the time of the acquisition

$$\Delta\phi_{i,k}^{mov} = \frac{4\pi}{\lambda_i}V_k t_i + \frac{4\pi}{\lambda_i}K_{dT,k}T_i \qquad (2.10)$$

---

[1]In the following, with no loss of generality, we neglect the subpixel position of the target, and we suppose that the radar target is in the center of the sampling cell. The interested reader should refer to [49] for a detailed analysis of subpixel positioning and its consequences on phase and amplitude of the received radar signal.
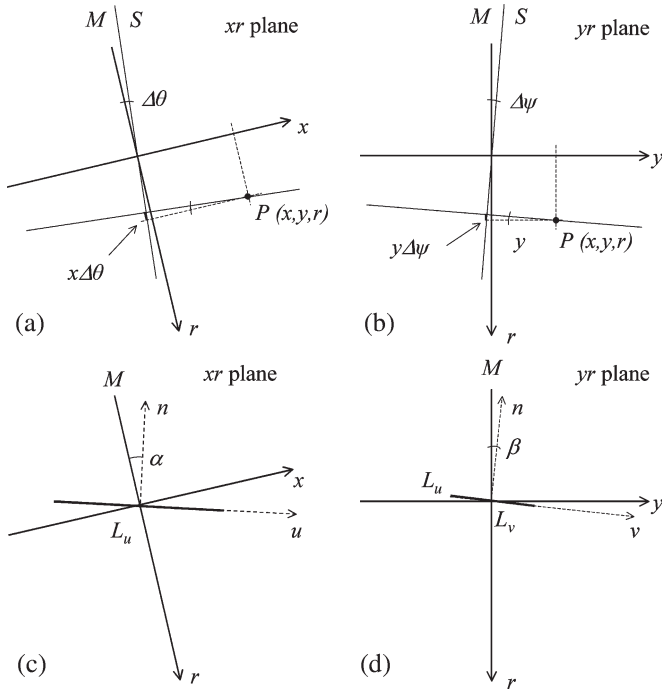
Fig. 2. (a), (b) Master acquisition geometry sections. (a) xr plane. (b) yr plane. The slave slant range direction is reported, forming two angles with the Master r-axis: (a) $\Delta\theta$ in xr plane and (b) $\Delta\psi$ in yr plane. Different view angles cause slightly different paths between sensor and target P localized by the coordinates (x, y, z). Angle $\Delta\theta$ causes a slant range path difference $x\Delta\theta$; angle $\Delta\psi$ generates $y\Delta\psi$. (c), (d) Target orientation in the Master acquisition geometry. (c) α: Angle between x-axis and u-axis. (d) β angle between y-axis and v-axis.

where V_k is the target velocity, and $K_{dT,k}$ is the proportionality constant displacement to temperature of target k.

Finally, the interferometric phase depends also on the radar-signal polarization. Here, we adopt a simplified model [45], [51] for the polarimetric behavior of our target. The target is expected to be visible both under VV and HH polarizations (also in AP mode with reduced azimuth spectra [50]), and the phase shift introduced by the different polarization is strictly connected to the target scattering mechanism

$$\Delta\phi_{i,k}^{\mathrm{pol}} = \phi_{\mathrm{pol},k}\eta_i. \qquad (2.11)$$

As well known in literature [51], the phase shift $\phi_{\mathrm{pol},k}$ between VV and HH polarizations ($\eta_i = 0$ and $\eta_i = 1$, respectively) is close to 0 for odd-bounce targets and close to π for even-bounce targets.

Thus, if we consider the interferometric phase of targets of small dimensions with respect to the resolution cell in our data set $\Delta\phi_{i,k} = \Delta\phi_{i,k}^{\mathrm{geo}} + \Delta\phi_{i,k}^{\mathrm{mov}} + \Delta\phi_{i,k}^{\mathrm{pol}}$, we are able to recover a first set of physical parameters that can be used to identify their 3-D position, the motion, as well as other information on their scattering mechanism. We then get the following characteristic vector $\mathbf{\Theta}_{\mathrm{phase}}$ for the targets under study:

$$\mathbf{\Theta}_{\mathrm{phase}} = [\Delta r, \Delta x, \delta y, V, K_{dT}, \phi_{\mathrm{pol}}]. \qquad (2.12)$$

2) Amplitude Analysis: By calculating the average amplitude $a_k = (1/N_I) \sum_{i=1}^{N_I} |s_{i,k}|$ of the radar images (supposed

to be radiometrically corrected), in correspondence of the pointwise target k (2.8), by means of the calibration constant K_{cal} [52], we can evaluate the radar cross section $\mathrm{RCS}_k = a_k^2 K_{\mathrm{cal}}$ [53], which is a useful information on the target physical nature. The scattering pattern of a pointwise target, in fact, is expected to be constant as a function of the previously described acquisition parameters, as evident from (2.8). A distributed target, on the other side, can exhibit a more complex behavior. In the following, we analyze the amplitude variation of a distributed target as a function of the acquisition geometry, frequency, temperature, and time by adopting a very simple but effective model.

Acquisition Geometry: We first study the variations of the monostatic RCS of a coherent radar target as a function of the acquisition geometry (more precisely the direction of propagation of the incident wave, which is described by normal baseline and DC frequency). The amplitude variations as a function of the look angle can be ascribed to the physical dimensions of the scattering object. In our discussion, we consider a very simple model for the target: a flat surface (i.e., a mirror) in a low-clutter environment. More precisely, we assign to the scatterer under investigation the size of an equivalent mirror with the same amplitude variations.

The target k, as in the pointwise case, is again modeled as the sum of a high number of elementary point targets. This time, the elementary scatterers are supposed to be uniformly distributed on a planar surface of extension $L_u \times L_v$ oriented as vector $\vec{n}$ [Figs. 1(b) and 2(c)–(d)]. For the sake of simplicity, the reflectivity value σ of the elementary point scatterers is assumed to be constant $\sigma = \sigma_0$. Here, we omit index k to lighten the notation.

The complex value s_i of image i in correspondence of the target can then be approximated as the sum of the elementary reflectivities

$$s_i \simeq \int \int \int \sigma(r, x, y) e^{-j\frac{4\pi}{\lambda_i} R_i} dr\, dx\, dy \qquad (2.13)$$

where R_i is the distance between the sensor in acquisition i and the scatterers having coordinates r, x, and y in the local reference system. More precisely

$$R_i = R_0 + r_i \simeq R_0 + r - x\Delta\theta_i - y\Delta\psi_i \qquad (2.14)$$

where the last equation highlights the dependence of R_i on the acquisition geometry $(\Delta\theta_i, \Delta\psi_i)$ of image i and the position of each elementary scatterer $P(x, y, r)$ [Fig. 2(a) and (b)]. To keep mathematics as simple as possible, in (2.13), the system impulse response has been supposed to be constant within the resolution cell. The approximation does not impact significantly on the final result since the target at hand is expected to be small with respect to the resolution cell (the results shown in Section III confirm the hypothesis).

Since the scatterers belong to a surface, (2.13) can be written as a double integral. With reference to Fig. 2(c) and (d), we have $x = u\cos\alpha$, $y = v\cos\beta$, and $r = u\sin\alpha + v\sin\beta$, where α is

the angle between u and x axes, and β is the angle between v and y axes. Equation (2.13) becomes

$$s_i \simeq \sigma_0 e^{-j\frac{4\pi}{\lambda_i}R_0}$$

$$\int_{-\frac{L_v}{2}}^{\frac{L_v}{2}} \int_{-\frac{L_u}{2}}^{\frac{L_u}{2}} e^{-j\frac{4\pi}{\lambda_i}(u\sin\alpha + v\sin\beta - u\Delta\theta_i\cos\alpha - v\Delta\psi_i\cos\beta)}\,du\,dv.$$

$$(2.15)$$

Recalling the Fourier transform of a rectangle

$$\int_{-\frac{\Delta}{2}}^{\frac{\Delta}{2}} e^{-j2\pi\xi\tau}\,d\tau = \Delta\frac{\sin(\pi\Delta\xi)}{\pi\Delta\xi} = \Delta\mathrm{sinc}(\Delta\xi) \qquad (2.16)$$

the pixel amplitude $a_i = |s_i|$ of image i can be written as

$$a_i \simeq |\sigma_0|L_u L_v \left| \frac{\sin\left[\frac{2\pi}{\lambda_i}L_u(\sin\alpha - \Delta\theta_i\cos\alpha)\right]}{\frac{2\pi}{\lambda_i}L_u(\sin\alpha - \Delta\theta_i\cos\alpha)} \right.$$

$$\left. \times \frac{\sin\left[\frac{2\pi}{\lambda_i}L_v(\sin\beta - \Delta\psi_i\cos\beta)\right]}{\frac{2\pi}{\lambda_i}L_v(\sin\beta - \Delta\psi_i\cos\beta)} \right| \qquad (2.17)$$

$$a_i \simeq \sqrt{\mathrm{RCS_{max}}} \left| \mathrm{sinc}\left[\frac{2}{\lambda_i}L_x(\theta_p - \Delta\theta_i)\right] \right.$$

$$\left. \times \mathrm{sinc}\left[\frac{2}{\lambda_i}L_y(\psi_p - \Delta\psi_i)\right] \right|. \qquad (2.18)$$

In (2.18), the variable $\mathrm{RCS_{max}}$ is the peak of the target RCS at the operating frequency of the radar, and it depends on the physical dimensions (L_u and L_v) and on the absolute value of the reflectivity. The variations of the amplitude values as a function of $\Delta\theta_i$ and $\Delta\psi_i$ then depend on the target dimensions projected in cross-slant range and azimuth ($L_x = L_u\cos\alpha$ and $L_y = L_v\cos\beta$), while the location of the maxima of the cardinal sines is related to the target orientation ($\theta_p = \tan\alpha$ and $\psi_p = \tan\beta$).

If we abstract (2.18) from the context of a mirror, we can exploit it for describing a little portion of the scattering pattern of a general target behaving as PS. If we consider $\mathrm{RCS_{max}}$ to be independent of the dimensions L_x and L_y, the scattering pattern, e.g., of a corner reflector, can be approximated by (2.18) with $L_x = 0$ and $L_y = 0$. In another condition, if we separate the pattern peak position θ_p, ψ_p from the target orientation α, β, (2.18) can be used for describing, for example, a resonating structure (Bragg scattering) not orthogonal to the line of sight (LOS) (e.g., a horizontal target $\alpha = \theta_0$ resonating in the direction θ_p).

Finally, (2.18) can be rewritten as a function of normal baseline and DC variation by exploiting (2.4) and (2.5)

$$a_i \simeq \sqrt{\mathrm{RCS_{max}}} \left| \mathrm{sinc}\left(\frac{2L_x(B_{n,i} - B_{np})}{R_0\lambda_i}\right) \right.$$

$$\left. \times \mathrm{sinc}\left[\frac{L_y}{\delta_{\mathrm{az}}}\left(\frac{\Delta f_{\mathrm{DC},i}}{\mathrm{PRF}} - \overline{\Delta f}_{\mathrm{DC}p}\right)\right] \right| \qquad (2.19)$$

where B_{np} and $\overline{\Delta f}_{\mathrm{DC}p}$ are the target pointing variables in cross-slant range and azimuth in terms of normal baseline (in meters) and PRF replicas of DC frequency (in hertz per PRF).

Acquisition Frequency: We consider now the dependence of the amplitude values on the acquisition frequency. The coherent combination of SAR data acquired with slightly different operating frequencies has been described in [5], where ERS and Envisat images have been jointly exploited in a PS analysis. Here, we study the impact on the amplitude of the radar signal. Although this analysis will not be used to recover further information on the target, it is useful for the sake of completeness.

If image i is acquired with a frequency shift Δf_i with respect to the Master acquisition $f_i = f_0 + \Delta f_i$, from (2.17), we obtain

$$a_i \simeq \varepsilon \left| \mathrm{sinc}\left[\frac{2}{c}L_u(f_0 + \Delta f_i)(\sin\alpha - \Delta\theta_i\cos\alpha)\right] \right| \quad (2.20)$$

where c is the speed of light, and ε gathers all amplitude factors independent of the frequency. If $\Delta f_i \ll f_0$, we can neglect the cross-product between frequency and angle changes Δf_i and $\Delta\theta_i$, respectively, obtaining

$$a_i \simeq \varepsilon \left| \mathrm{sinc}\left[\frac{2}{c}(f_0 L_u\sin\alpha - f_0\Delta\theta_i L_u\cos\alpha + \Delta f_i L_u\sin\alpha)\right] \right|.$$

$$(2.21)$$

The argument of the sinc function in (2.21) is the sum of three terms. The first one ($f_0 L_u\sin\alpha$) is independent of frequency and look-angle changes: it identifies the position of the peak of the sinc function in the parameter space $\Delta f_i, \Delta\theta_i$, and it depends on the mirror pointing angle α. The second one ($f_0\Delta\theta_i L_u\cos\alpha$) is a function of the view-angle difference $\Delta\theta_i$ and the cross-slant range projection of the target length $L_x = L_u\cos\alpha$. Finally, ($f_i L_u\sin\alpha$) takes into account the different frequency and the target dimension projected on the range direction.

Equation (2.21) states also an equivalence between baseline (proportional to $\Delta\theta_i$) and frequency variation Δf_i. In fact, for a flat surface, a frequency shift can be compensated by changing the look angle accordingly: It is just another way to state the wavenumber-shift principle [5], [54]

$$f_0\Delta\theta_i L_u\cos\alpha = \Delta f_i L_u\sin\alpha. \qquad (2.22)$$

In [5], the frequency–angle equivalence is exploited for explaining the PS survival rate, passing from ERS–ERS to ERS–Envisat interferograms, under the hypothesis that surface scatterers can be considered, on the average, horizontal ($\alpha = \theta_0$).

Temperature: The impact on the RCS of a thermal dilation of the target due to different temperatures at the time of acquisitions is mathematically similar to a frequency shift. In fact, the expansion of an object of length L_0 can be described, as a first approximation, by a linear relationship

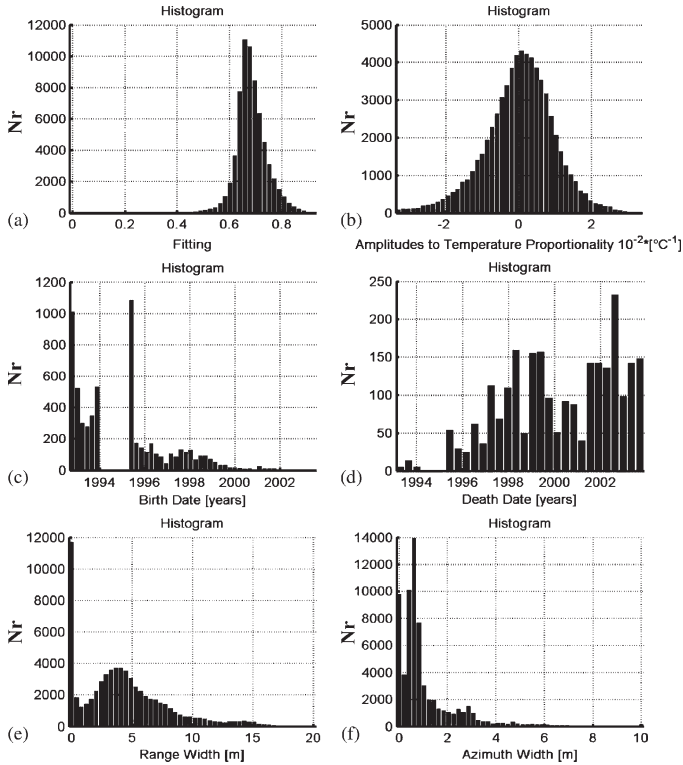$$\Delta L = \zeta L_0\Delta T. \qquad (2.23)$$

Fig. 3. Histograms of estimated amplitude parameters for the 60 000 PSs detected in Milan with coherence $\gamma > 0.7$. (a) Fitting index $\hat{\xi}_{\text{fit}}$ (2.32). (b) Temperature–amplitude coefficient $\hat{K}_{\text{aT}}$. About 7000 (12%) PSs with $|\hat{K}_{\text{aT}}| > 1.5 \cdot 10^{-2}$ $^\circ\text{C}^{-1}$ can be recognized as backscattering targets. (c) Birth date $\hat{t}_{\text{ON}}$. About 9000 (15%) PSs started working after the first acquisition in the data set (May 16, 1992). (d) Death date $\hat{t}_{\text{OFF}}$. About 2000 (3%) PSs faded away during the 13-year time span before the last data-set image (July 6, 2004). (e) Cross-slant range width $\hat{L}_x$. About 10 000 (17%) PSs have cross-slant range width $\hat{L}_x < 0.1$ m. (f) Azimuth width $\hat{L}_y$. About 9000 (15%) PSs have azimuth width $\hat{L}_y < 0.1$ m.

A temperature change ΔT causes a dilation ΔL. As well known, the constant ζ is called the coefficient of linear expansion and depends on the material affected by the temperature variation. Given an object of length $L_0 = 2$ m, with a thermal expansion coefficient $\zeta = 2.5 \cdot 10^{-5}$ $^\circ\text{C}^{-1}$ (aluminum) and a temperature change of 30 $^\circ$C, the thermal dilation is about $\Delta L = 1.5$ mm.

In order to quantify the impact of a possible thermal dilation of the target on the amplitude of the radar signal, we insert the linear expansion formula (2.23) in our scattering model (2.17). For the sake of simplicity, we analyze only the range dimension. Equation (2.17) then becomes

$$a_i \simeq \varepsilon(L_{u0} + \Delta L_{u,i}) \left| \text{sinc} \left[\frac{2}{\lambda}(L_{u0} + \Delta L_{u,i}) \right. \right.$$

$$\left. \left. \times (\sin\alpha - \Delta\theta_i \cos\alpha) \right] \right|. \quad (2.24)$$

It is easy to recognize that the change of scattering surface due to the thermal dilation is not sufficient to create a significant variation of the maximum of the sinc function: $\varepsilon(L_{u0} + \Delta L_{u,i}) \simeq \varepsilon L_{u0}$. However, the argument of the cardi-

nal sine can change, and the RCS is modulated accordingly. Equation (2.24) can be rewritten as

$$a_i \simeq \varepsilon L_{u0} \left| \text{sinc} \left[\frac{2}{\lambda}(L_{u0}\sin\alpha + \Delta L_{u,i}\sin\alpha - L_{u0}\Delta\theta_i\cos\alpha) \right] \right|$$

$$(2.25)$$

where we neglected the cross-product between the view-angle and temperature changes. Equation (2.25) states that an increase of size $\Delta L_{u,i}$ has an impact similar to a view-angle change $\Delta\theta_i$. A temperature variation ΔT_i modifies the target RCS proportionally to the range projection of the target length $L_{r0} = L_{u0}\sin\alpha$ [similarly to a frequency shift in (2.21)]: $\Delta L_{u,i}\sin\alpha = \zeta\Delta T_i L_{r0}$. This implies that a mirror orthogonal to the LOS ($\alpha = 0$) is unaffected by temperature-dependent amplitude variations. Targets with a significant seasonal variation of the RCS are usually distributed objects that scatter a significant portion of the radar signal back to the sensor, like periodic structures (Bragg scattering) not orthogonal to the LOS, which resonate in the radar direction.

In order to quantify the thermal-dilation effect, we can compare the last two terms in the sinc argument of (2.25)

$$\zeta\Delta T_i L_{u0}\sin\alpha = L_{u0}\Delta\theta_i\cos\alpha. \quad (2.26)$$

According to (2.26) for a horizontal target ($\alpha = \theta_0$) with $\zeta = 2.5 \cdot 10^{-5}$ $^\circ\text{C}^{-1}$, 30 $^\circ$C of temperature corresponds to about 270 m of normal baseline.

Empirically, rather than using a complex analytical formulation, we found that a reasonable model can be obtained by introducing a coefficient K_{aT} of linear dependence between amplitude and temperature and by adopting the following simple equation describing the amplitude variation of a target affected by a temperature change ΔT:

$$\Delta a = K_{\text{aT}}a\Delta T. \quad (2.27)$$

Consequently, our scattering model becomes

$$a'_i = a_i(1 - K_{\text{aT}}\Delta T_i) \quad (2.28)$$

where a_i is given by (2.19), and ΔT_i is the temperature difference between image i and the Master one. The amplitude–temperature coefficient K_{aT} (per degree Celsius) depends on the target material, dimensions, and orientation and can be exploited for identifying resonating targets.

Time: In long temporal series of SAR data covering many years, it can happen that a pixel exhibits PS behavior only within a certain temporal window, i.e., in a subset of images. In this case, abrupt changes in the time series of the RCS values are usually clearly visible [55]. Focusing on man-made structures and neglecting more complex variations of the RCS values, we model the target life cycle by means of two variables: t_{ON} and t_{OFF}. More precisely, the amplitude model a'_i of image i (2.28) is multiplied by a boxcar function, so that the analysis is focused on a subset of the multitemporal data set

$$a''_i = a'_i \text{rect}_{t_{\text{ON}}, t_{\text{OFF}}}(t_i). \quad (2.29)$$

In (2.29), t_i is the temporal baseline of image i. In other words, we suppose that the reflectivity values outside the "PS window"

are negligible with respect to the RCS of the coherent scatterer under different aspect angles.

Concluding the amplitude analysis, we can sum up in the target characteristic vector $\Theta_{\text{amplitude}}$ the variables used for describing our model

$$\boldsymbol{\Theta}_{\text{amp}} = [\text{RCS}, L_x, \theta_p, L_y, \psi_p, K_{\text{aT}}, t_{\text{ON}}, t_{\text{OFF}}]. \quad (2.30)$$

C. Inverse Problem

In the previous sections, we derived the vector $\boldsymbol{\Omega}_i$ of the degrees of freedom of image i, the target characteristics vector $\boldsymbol{\Theta}_k$ of target k, and the model for the complex signal $s_{i,k} = a_{i,k}e^{j\phi_{i,k}}$ as a function of $\boldsymbol{\Omega}_i$ and $\boldsymbol{\Theta}_k$. In order to estimate the target characteristics $\boldsymbol{\Theta}_k$, we consider separately the amplitude and phase of the complex signal. For the phase domain, we proceed as in the classical PS analysis by finding the maximum of the periodogram (the temporal coherence) as a function of $\boldsymbol{\Theta}_{\text{phase},k}$ [1]

$$\gamma_k = \frac{1}{N_I} \left| \sum_{i=1}^{N_I} e^{j\left[\Delta\phi_{i,k}^{\text{rec}} - \Delta\phi_{i,k}(\boldsymbol{\Theta}_{\text{phase},k})\right]} \right| \quad (2.31)$$

where $\Delta\phi_{i,k}^{\text{rec}}$ is the interferometric phase of the received signal. The problem is nonlinear, and it can be solved either by systematically searching the parameter space for the desired solution or by means of an optimization method such as the gradient. We implemented the gradient method, taking into account an *a priori* information on the analyzed data set. The temporal coherence γ_k is an index of the reliability of the estimate.

For the amplitude domain, both the function to be optimized and the algorithm to be applied for the parameter estimation should be carefully selected. The cost function (i.e., the norm adopted to describe the matching between the data and the model) should take into account the presence of possible statistical outliers due to clutter: Robust norms are preferable with respect to standard LMS fitting. Moreover, since the system is highly nonlinear, the computational burden should be studied in detail since the area of interest can have hundreds of thousands of PSs to be analyzed. We chose the following objective function to be maximized for target k:

$$\xi_{\text{amp},k} = 1 - \frac{\sum_i \left| a_{i,k}^{\text{rec}} - a_i(\boldsymbol{\Theta}_{\text{amp},k}) \right|}{\sum_i \left| a_{i,k}^{\text{rec}} \right|} \quad (2.32)$$

where $a_{i,k}^{\text{rec}}$ are the received amplitude data, a_i are the model values as a function of the target characteristics $\boldsymbol{\Theta}_{\text{amp},k}$, and the sum is carried out over the multitemporal data set. The fitting index $\xi_{\text{amp},k}$ is always lower than one and approaches one in case of perfect agreement between the model and data.

Note that under the assumption of pointwise scatterers, assuming amplitude values equal to a constant plus white Gaussian noise $a_{i,k}^{\text{rec}} = \mu_k + n_i(n_i \sim N(0, \sigma^2))$, the fitting index $\xi_{\text{amp},k} \simeq 1 - \sigma/\mu_k$ can be related to the amplitude stability index $S_{A,k} = (\mu_k/\sigma)$ [1]. Therefore, the fitting index (2.32) can be thought of as an advanced measure (L^1 rather than L^2

TABLE I

SUMMARY OF THE CHARACTERISTICS OF THE SIX RECOGNIZED TARGET TYPOLOGIES (+ MEANS GREATER, WHILE − MEANS LOWER). COLUMNS: CROSS-SLANT RANGE WIDTH $\hat{L}_x$, AZIMUTH WIDTH $\hat{L}_y$, AP PHASE $\hat{\phi}_{\text{pol}}$, RADAR CROSS SECTION $\widehat{\text{RCS}}$, TEMPERATURE–AMPLITUDE COEFFICIENT $\hat{K}_{\text{aT}}$, AND ELEVATION WITH RESPECT TO THE GROUND $\hat{h}$

	L_x	L_y	ϕ_{pol}	RCS	k_T	h
Roof	+	+	0	$\propto s_0 L_x L_y$	+	+
Grating	+	+	0	$\propto s_0 L_x L_y$	+	−
Dihedral	−	+	π	+	−	−
Resonating Dihedral	−	+	π	+	+	−
Pole	−	−	π	−	−	−
Trihedral	−	−	0	+	−	−

norm is adopted) of amplitude stability that takes into account the features of the multitemporal data set under study.

The final feature vector is then the result of a nonlinear optimization of eight parameters

$$\hat{\boldsymbol{\Theta}}_{\text{amp},k} = \arg\max(\xi_{\text{amp},k}). \quad (2.33)$$

Due to the complexity of the problem, no standard solution exists. We developed a genetic algorithm [56], but other strategies can be adopted. Our algorithm has been adapted to get a reasonable trade-off between processing speed and reliability, taking into account prior information that can drive the optimization, limiting the volume of the parameter space to be searched. Finally, it is important to point out that the higher the dispersion of baseline and DC values, the more reliable is the scattering pattern estimate and, therefore, the amplitude analysis.

D. Classification and Recognition

The classification procedure $g \colon \boldsymbol{\Theta} \to \mathcal{X}$ consists in the assignment of a target class χ_k to the scatterer at hand, which is based on the estimated characteristics $\hat{\boldsymbol{\Theta}}_k = [\hat{\boldsymbol{\Theta}}_{\text{phase},k}, \hat{\boldsymbol{\Theta}}_{\text{amp},k}]$. In our paper, the real goal of such a task is the identification of the scattering structures that can be discerned from the estimated characteristic vector. The results described in the following have been achieved through the assiduous observation of the georeferenced radar data together with high-resolution optical images and *in situ* surveys. Here, we briefly report the main characteristics for each target class; in the next section, we describe them through some meaningful examples.

1) Target Typologies: From the feature vectors described above and the analysis of real data sets, the six main target typologies that have been identified are the following:

1) Resonating scatterers as floor metal gratings: targets characterized by single-bounce scattering ($\phi_{\text{pol}} \simeq 0$), ground elevation, and finite dimensions both in azimuth and cross-slant range direction. Sensitivity to temperature of RCS but not of LOS displacement. RCS values dependent on their physical dimensions.

2) Roofs: targets characterized by single-bounce scattering ($\phi_{\text{pol}} \simeq 0$), high elevation, and finite dimensions both in
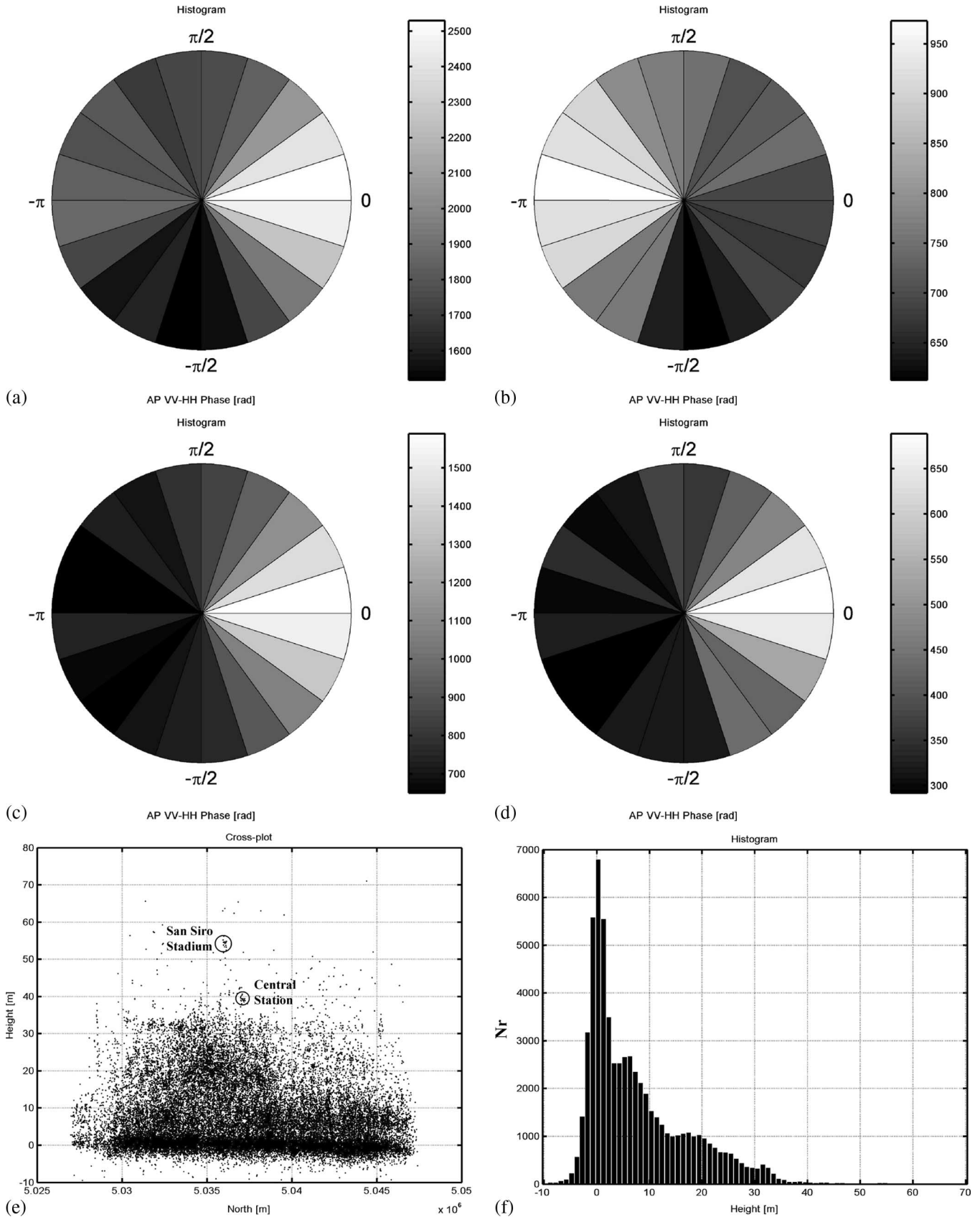
Fig. 4. Pie histograms of AP phase for different PS classes. (a) About 7500 PSs have AP phase around $\pi(|\hat{\phi}_{\mathrm{pol}}| > 2.5$ rad), and 10 000 PSs have AP phase $|\hat{\phi}_{\mathrm{pol}}| < 0.6$ rad. (b) 15 000 PSs on the ground (elevation $|\hat{h}| < 3$ m) are principally dihedrals (AP-phase peak on π rad). (c) 20 000 PSs at high elevation ($\hat{h} > 5$ m) have odd-bounce scattering system with high probability (AP-phase peak on 0 rad). (d) 7000 PSs with temperature–amplitude coefficient $|\hat{K}_{\mathrm{aT}}| > 1.5 \cdot 10^{-2}\ {}^{\circ}\mathrm{C}^{-1}$ (backscatterers) have a neat prevalence of odd bounces (AP-phase peak on 0 rad). (e) North–south profile of Milan City after removing for the low-pass topography. (f) Histogram of PS residual elevations (after removing for the low-pass topography) in Milan.

TABLE II

CLASSIFICATION RESULT IN THE MILAN URBAN SITE. FOR EACH
TARGET TYPOLOGY, THE PERCENTAGE OF TARGETS RECOGNIZED
BELONGING TO IT IS REPORTED IN THE RIGHT COLUMN

	%
Roof	50
Grating	11
Dihedral	13
Resonating Dihedral	7
Pole	11
Trihedral	8

azimuth and cross-slant range direction. Possible sensitivity of both LOS displacement and RCS with temperature. RCS values dependent on their physical dimensions.

3) Simple dihedrals: targets characterized by double-bounce scattering ($\phi_{\text{pol}} \simeq \pi$), ground elevation, negligible dimension in cross-slant range, and finite dimension in azimuth. Negligible sensitivity of both LOS displacement and RCS with temperature. RCS values usually high.

4) Resonating dihedrals as metal fences: targets characterized by double-bounce scattering ($\phi_{\text{pol}} \simeq \pi$), ground elevation, and finite dimensions both in azimuth and cross-slant range direction. Sensitivity to temperature of RCS but not of LOS displacement. Middle-low RCS values.

5) Poles: targets characterized by double-bounce scattering ($\phi_{\text{pol}} \simeq \pi$), ground elevation, and negligible dimension in both cross-slant range and azimuth. Negligible sensitivity of both LOS displacement and RCS with temperature. RCS values usually rather low.

6) Trihedrals: targets characterized by triple-bounce scattering ($\phi_{\text{pol}} \simeq 0$), ground elevation, and negligible dimension in both cross-slant range and azimuth. Negligible sensitivity of both LOS displacement and RCS with temperature. RCS values usually high.

Table I summarizes, with the already mentioned symbol meaning, the characteristics of each kind of target.

The classification process can now be implemented by evaluating the distance in the $N_{\Theta} - D$ space between the point identified by $\hat{\mathbf{\Theta}}_k$ and the aforementioned classes. The distance can be properly adjusted by means of nonlinear functions in order to find the best fit between the result and the observed data. A good way to perform this task is the use of neural networks, but a discussion on the optimization of this stage is not the scope of the paper and will be the object of future efforts.

III. REAL-DATA ANALYSIS

In this section, we describe the results of the analysis on the physical nature of the PSs in the Milan urban site: first by reporting the statistics of the estimated parameters and then by showing meaningful examples of recognized targets. The exploited SAR data set is formed by $N_I' = 108$ ERS images and $N_I'' = 12$ Envisat images acquired from 1992 to 2005. The ERS image acquired on January 14, 1997 is selected as the Master scene, and all the slave acquisitions are resam-

pled on the common Master grid. The test area covers about 400 km^2. About 60 000 PSs with coherence $\gamma > 0.7$ [1] have been detected in the Milan site.

A. Statistics and Classification Results

Fig. 3 shows the histograms of fitting index $\hat{\varepsilon}_{\text{fit}}$ (a), amplitude–temperature coefficient $\hat{K}_{\text{aT}}$ (b), birth date $\hat{t}_{\text{ON}}$ (c), death date $\hat{t}_{\text{OFF}}$ (d), range width $\hat{L}_x$ (e), and azimuth width $\hat{L}_y$ (f) estimated in the Milan site. About 9000 (15%) PSs started working after the first acquisition in the data set (May 16, 1992), and about 2000 (3%) PSs faded away during the 13 years time span before the last data-set image (September 14, 2004). About 7000 (12%) PSs with amplitude–temperature coefficient $|\hat{k}_{\text{T}}| > 1.5 \cdot 10^{-2}$ °C^{-1} can be recognized as backscattering targets. From the histograms of the physical dimensions, it is interesting to observe that pointwise targets (peak at zero width) in cross-slant range and azimuth are neatly distinguished from the other scatterers. About 10 000 (17%) PSs have cross-slant range width $\hat{L}_x < 0.1$ m, and about 9000 (15%) PSs have azimuth width $\hat{L}_y < 0.1$ m. Only 1500 (2.5%) PSs are characterized by both dimensions smaller than 0.1 m. Furthermore, it can be seen that the system is much more selective in azimuth than in range (azimuth widths are much smaller than cross-slant range widths).

Fig. 4 shows the polarimetric behavior of the coherent targets in Milan as estimated from the autointerferometric phase of an Envisat AP acquisition. Fig. 4(a) is the histogram of the AP phase for the detected PSs. About 7000 PSs have AP phase around $\pi(|\hat{\phi}_{\text{pol}}| > 2.5$ rad) revealing a double-bounce mechanism; 10 000 PSs have AP phase $|\hat{\phi}_{\text{pol}}| < 0.6$ rad (odd-bounce). The AP phase of the rest of PSs has a slight positive prevalence. It is interesting to connect the AP phase with two other estimated PS parameters: elevation and amplitude temperature dependence. Fig. 4(e) shows the PS elevation with respect to the ground in Milan City as a function of the north coordinate, and Fig. 4(f) is the elevation distribution. As clearly visible, the highest density of PSs in an urban site is at street level [49]. Fig. 4(b) and (c) shows two AP-phase histograms for two PS-elevation classes. PSs on the ground [Fig. 4(b)] with elevation $|\hat{h}| < 3$ m (15 000 points) are principally dihedrals, while at higher elevation with $\hat{h} > 5$ m (Fig. 4(c), 20 000 PSs), odd bounces dominate (tiled roofs or corrugated iron roofs are good backscatterers). By evaluating then the correlation between the AP phase and the temperature–amplitude coefficient $\hat{K}_{\text{aT}}$ in Fig. 4(d), we discover a neat prevalence of single-bounce scatterers for the 7000 PSs with temperature–amplitude coefficient $|\hat{K}_{\text{aT}}| > 1.5 \cdot 10^{-2}$ °C^{-1}.

The results of the classification described in the previous section and based on the estimated parameters are shown in Table II. For each target typology previously described, the percentage of Milan PSs recognized belonging to it is reported. The typology with highest percentage is "roof" (50%); the remaining classes are all more or less about 10%. The results have been precisely georeferenced and compared with optical data. However, even high-resolution airborne images are not enough to allow a reliable cross-validation of the recognition of the scattering typologies. To achieve the aim, we took
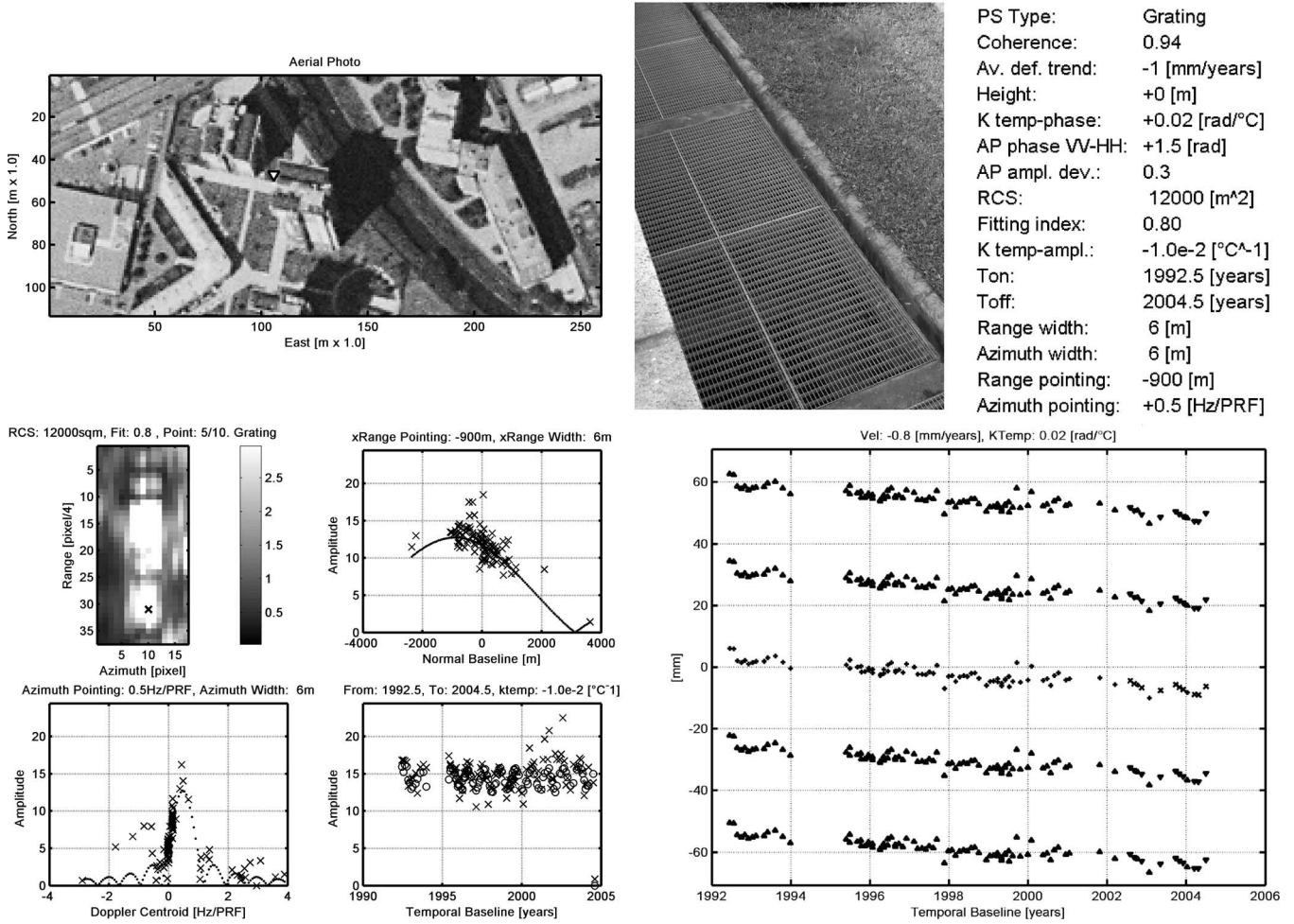
Fig. 5. Example of PS recognized as a grating. The target lies on the ground ($\hat{h} = 0$ m), it is extended ($\hat{L}_x = 6$ m and $\hat{L}_y = 6$ m), the amplitude has a temperature dependence ($\hat{K}_{aT} = -1.10^{-2}$ °C^{-1}), the peak RCS is high ($\widehat{RCS} = 12\,000$ m^2), and the amplitude estimate is reliable ($\hat{\xi}_{fit} = 0.8$). AP phase not so significant ($\hat{\phi}_{pol} = 1.5$ rad). The target has a good coherence ($\gamma = 0.94$), and the average deformation trend is slightly negative ($\hat{V} = -1$ mm/year).

advantage of the many pictures of detected targets collected *in situ*. Some examples of the validation are reported in the next section, together with a detailed description of the observed target typologies. From the collected observations and by analyzing the reliability indexes, it can be stated that, whenever the distance between the PS parameters and the estimated class is small (30% of PSs in Milan), the accuracy of the classification is higher than 90%.

B. Target Examples

Fig. 5 and the following report some examples of the target typologies detected in the urban site of Milan. Each figure is organized as follows. Up on the left, an aerial photo in the Gauss–Boaga coordinate system is reported, together with the PS position, which is identified by a black bordered white triangle. Please note that perspective effects can shift the visualized position of elevated objects (as roofs) from the actual one, leading sometimes to a misunderstanding of the PS geolocation. The radar is flying from north to southwest (descending pass), and it is right-looking. Up on the right, the target type detected by the system and a list of the estimated parameters are shown. Down on the left, the amplitude series is plotted, together

with the reflectivity map, with a cross on the PS pixel. The scattering pattern is plotted as a function of the following (clockwise): normal baseline (in meters); temporal baseline (in years); and DC frequency (in hertz per PRF). The measured amplitude is plotted with a cross, while the estimated model is represented with dots (circles). Finally, down on the right, the target displacement (in millimeters) (with respect to a reference point in Milan) is depicted as a function of the acquisition date (+ ERS and × Envisat data). The displacement series has been replicated at different ambiguities for a better visualization (^ ERS and v Envisat data).

1) Ground and Elevated Backscatterers: The most common urban SAR targets are flat backscatterers (about 60% in Milan). Among them, there are mirrors (very rare due to the strict requirement on the pointing), resonating structures (as floor metal gratings), roofs (tiled roofs and corrugated iron roofs), and curved surfaces (as domes or shed roofs). Their main characteristics are as follows: AP phase toward zero radians; amplitude dependence on temperature (except rare mirrors orthogonal to the LOS); dimensions of the equivalent mirror higher than zero; and middle-high values of peak RCS (proportional to the dimensions). Floor gratings can be distinguished from roof-like scatterers by means of the elevation with respect

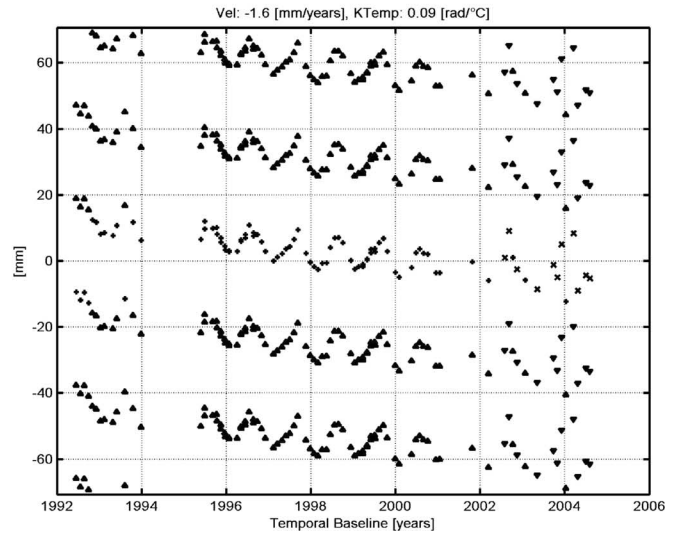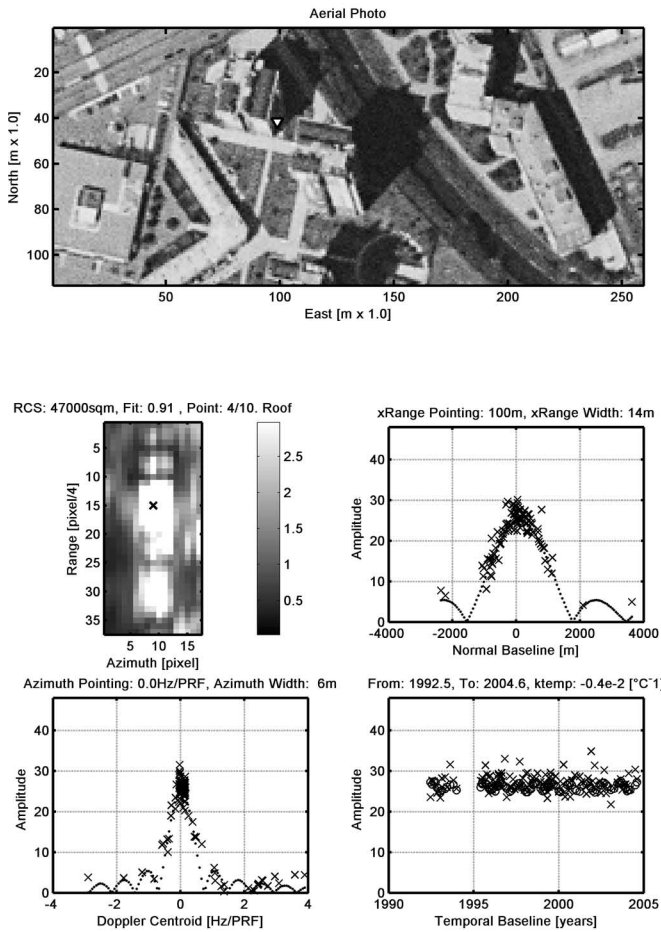| PS Type:	Roof
Coherence:	0.97
Av. def. trend:	-2 [mm/years]
Height:	+38 [m]
K temp-phase:	+0.09 [rad/°C]
AP phase VV-HH:	+0.5 [rad]
AP ampl. dev.:	0.3
RCS:	47000 [m^2]
Fitting index:	0.91
K temp-ampl.:	-0.4e-2 [°C^-1]
Ton:	1992.5 [years]
Toff:	2004.6 [years]
Range width:	14 [m]
Azimuth width:	6 [m]
Range pointing:	+100 [m]
Azimuth pointing:	+0.0 [Hz/PRF]

Fig. 6. Example of PS recognized as a roof. The target is at $\hat{h} = 38$ m from the ground, very extended ($\hat{L}_x = 14$ m and $\hat{L}_y = 6$ m), with high radar return ($\widehat{RCS} = 47\,000$ m^2), with low temperature dependence ($\hat{k}_T = -0.4 \cdot 10^{-2}$ °C^{-1}), and with high amplitude reliability ($\hat{\xi}_{fit} = 0.91$). AP phase close to zero ($\hat{\phi}_{pol} = 0.5$ rad). In comparison with the grating of Fig. 5, the roof shows that the building has a subsidence rate ($\hat{V} = -2$ mm/year) higher than the surrounding terrain (likely structural stabilization). Knowing the target scattering nature, the measured deformation can be correctly interpreted [4].

to the ground. In addition, general distributed flat scatterers (as rough surfaces) are present but usually with low RCS and low signal-to-noise ratio (SNR).

Fig. 5 shows a PS recognized by the system as a floor grating. The target lies on the ground ($\hat{h} = 0$ m), it is extended ($\hat{L}_x = 6$ m and $\hat{L}_x = 6$ m), the amplitude has a temperature dependence ($\hat{k}_T = -1 \cdot 10^{-2}$ °C^{-1}), the peak RCS is high ($\widehat{RCS} = 12\,000$ m^2), and the amplitude estimate is reliable ($\hat{\varepsilon}_{fit} = 0.8$). The AP phase in this case is not significant ($\phi_{pol} = 1.5$ rad). The target has a good coherence ($\gamma = 0.94$), and the average deformation trend is slightly negative ($\hat{V} = -1$ mm/year).

Fig. 6 shows a PS very close to the grating just seen, but the system recognizes it as a roof. The target is at $\hat{h} = 38$ m from the ground, very extended ($\hat{L}_x = 14$ m and $\hat{L}_y = 6$ m), with high radar return ($\widehat{RCS} = 47\,000$ m^2), with low temperature dependence ($\hat{k}_T = -0.4 \cdot 10^{-2}$ °C^{-1}), and with high amplitude reliability ($\hat{\varepsilon}_{fit} = 0.91$). The AP phase is, as expected, close to zero ($\hat{\phi}_{pol} = 0.5$ rad). The PS has a very high coherence ($\gamma = 0.97$). What is really interesting in this example is the target displacement. The roof has a northeast location very similar to the grating in Fig. 5, but its displace-

ment is different. The grating shows that a slight subsidence is affecting the ground with respect to the reference point in Milan. The roof shows that the building has a subsidence rate ($\hat{V} = -2$ mm/year) higher than the surrounding terrain (likely structural stabilization). Moreover, the roof has a thermal dilation proportional to the building height (see [49]). This example highlights the importance of target identification and classification for a correct interpretation of deformation phenomena.

2) Dihedrals: Dihedral-type scatterers are the second most frequent target typology in urban sites (about 30% in Milan, considering simple dihedrals, fences, and poles). The main electromagnetic characteristic of a dihedral is the double-bounce scattering mechanism. Such a property can be detected by analyzing the polarimetric phase. A value of AP phase close to π radians reveals the double-bounce nature of the target at hand. Dielectric faces, however, can modify the phase delay of the reflected signal. A simple dihedral is usually formed by a building wall and the ground (low PS elevation), but there are also elevated dihedrals consisting of building right-angled structural details. A classical dihedral has the edge orthogonal to the LOS, which is parallel to the flight direction. Nevertheless, also dihedrals not parallel to the azimuth direction have
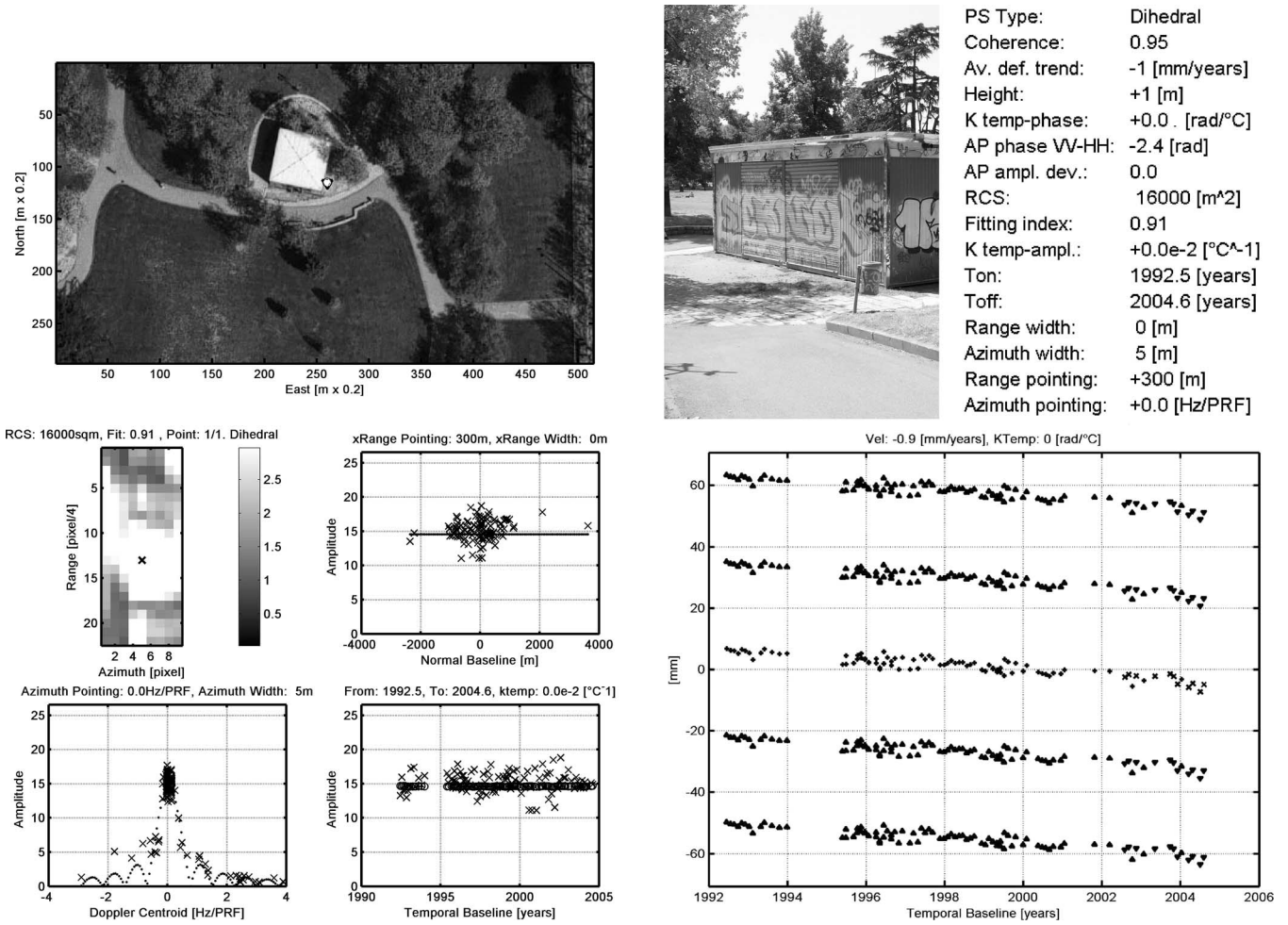
PS Type:	Dihedral
Coherence:	0.95
Av. def. trend:	-1 [mm/years]
Height:	+1 [m]
K temp-phase:	+0.0 [rad/°C]
AP phase VV-HH:	-2.4 [rad]
AP ampl. dev.:	0.0
RCS:	16000 [m^2]
Fitting index:	0.91
K temp-ampl.:	+0.0e-2 [°C^-1]
Ton:	1992.5 [years]
Toff:	2004.6 [years]
Range width:	0 [m]
Azimuth width:	5 [m]
Range pointing:	+300 [m]
Azimuth pointing:	+0.0 [Hz/PRF]

Fig. 7. Example of PS recognized as a dihedral. The target lies on the ground ($\hat{h} = 1$ m), and it has a quite high RCS ($\widehat{\mathrm{RCS}} = 16\,000$ m^2). The model fits very well the amplitude data ($\hat{\xi}_{\mathrm{fit}} = 0.91$), the estimated cross-slant range width is null ($\hat{L}_x = 0$ m), and the azimuth width is high ($\hat{L}_y = 5$ m). The dihedral has the edge perfectly perpendicular to the LOS (the estimated scattering pattern peak position as a function of DC-frequency difference is $\widehat{\Delta f}_{\mathrm{DC}p} = 0$ Hz/PRF). The phase series has a high coherence ($\gamma = 0.95$), and the associated displacement reveals a slight subsidence ($\hat{V} = -1$ mm/year). The AP information is in accordance with the theory (AP phase $\hat{\phi}_{\mathrm{pol}} = -2.4$ rad). Dihedrals can be used for connecting data acquired from parallel tracks [6].

been observed. This is the case, e.g., of metal fences (vertical structures consisting of periodic elements) that resonate in the radar LOS and that interact with the terrain forming a double-bounce system. We call this kind of scatterers "resonating dihedrals." Resonating dihedrals (about 7% in Milan) can be distinguished from the classical ones by analyzing the dependence of the amplitude of the received radar signal on the temperature. A resonating target, in fact, as previously shown, is sensitive to thermal dilation. The cross-slant range width of a dihedral is theoretically zero (the scattering pattern is constant along the normal baseline, and the target behaves as a pointwise scatterer), but the possible presence of more scattering centers on the building façade can sometimes cause an apparent nonnull extension. The azimuth width of a dihedral is higher than zero, and the square root of the RCS is proportional to it.

Fig. 7 shows a target example recognized by the system as a classical dihedral. The target lies on the ground ($\hat{h} = 1$ m), and it has a quite high RCS ($\widehat{\mathrm{RCS}} = 16\,000$ m^2). The model fits very well the amplitude data ($\hat{\varepsilon}_{\mathrm{fit}} = 0.91$), the estimated cross-slant range width is null ($\hat{L}_x = 0$ m), and the azimuth width is high ($\hat{L}_y = 5$ m). The dihedral has the edge perfectly

perpendicular to the LOS (the estimated scattering pattern peak position as a function of DC frequency difference is $\widehat{\Delta f}_{\mathrm{DC}p} = 0$ Hz/PRF). The phase series has a high coherence ($\gamma = 0.95$), and the associated displacement reveals a slight subsidence ($\hat{V} = -1$ mm/year). The AP information is in accordance with the theory (AP phase $\hat{\phi}_{\mathrm{pol}} = -2.4$ rad).

Dihedrals have a wide scattering pattern as a function of normal baseline. This fact can be fruitfully exploited for connecting data coming from different parallel tracks or acquired with different carrier frequencies (see [5] and [6]).

3) Poles: Poles are a particular case of dihedrals with cylindric symmetry (about 10% in Milan). The azimuth width of a pole is practically null, and this fact has a consequence also on the RCS, which depends on its height and radius (not detected by the system). Thus, poles have usually low RCS and low SNR, and sometimes, they are not distinguished from other noisy weak scatterers. Expected pole radar parameters are the following: azimuth and range null dimensions; low RCS; AP phase toward π radians; low elevation with respect to the ground; and no temperature-dependent amplitude variation. A pole must respect two main conditions in order to be observable
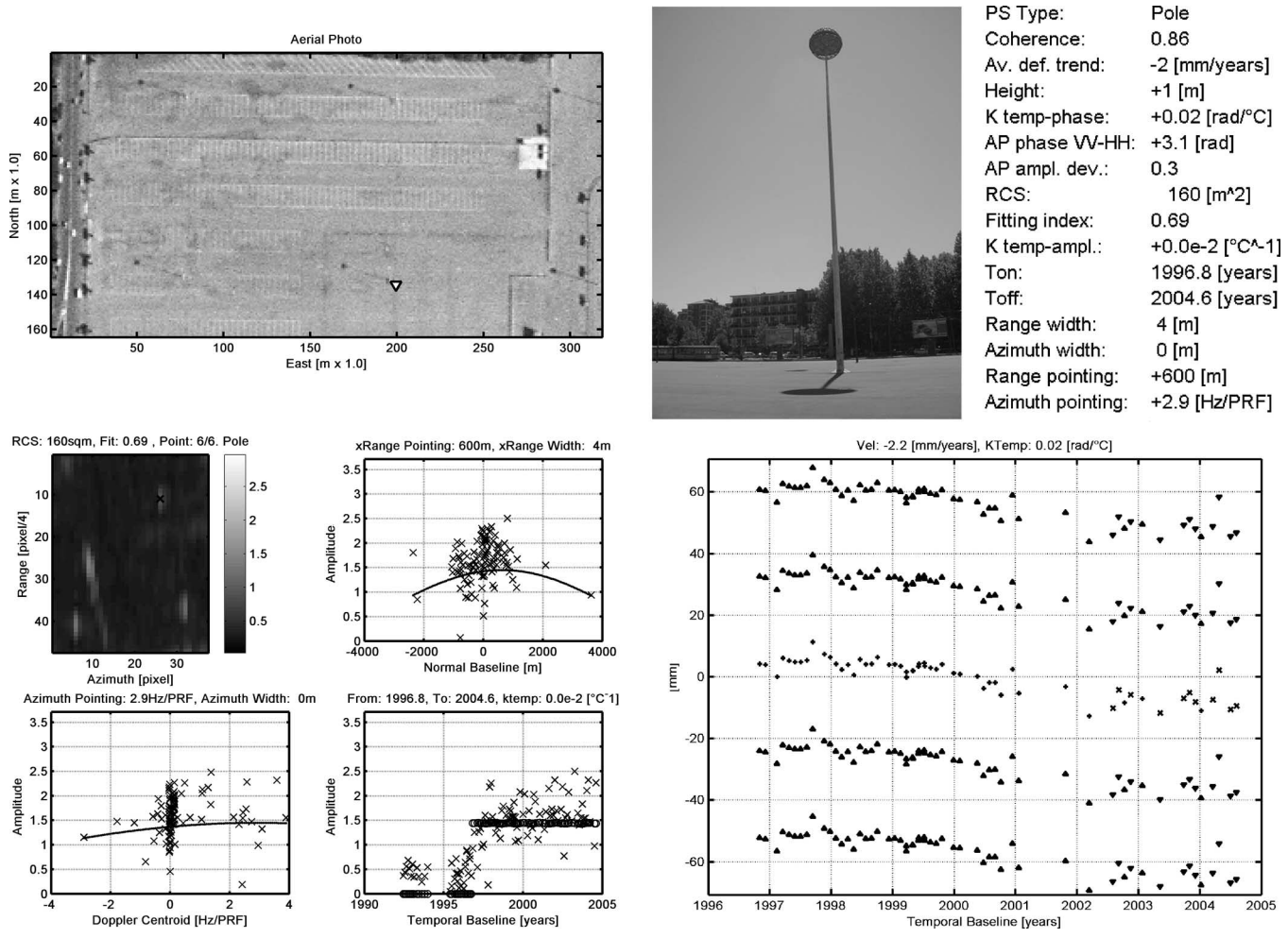
Fig. 8. Example of PS recognized as a pole (in a car park). The target has a very low RCS ($\widehat{\mathrm{RCS}} = 160\ \mathrm{m}^2$), and consequently, the amplitude model estimate is not reliable ($\hat{\xi}_{\mathrm{fit}} = 0.69$). The AP phase, on the contrary, is reasonable ($\hat{\phi}_{\mathrm{pol}} = 3.1\ \mathrm{rad}$). As visible from the amplitude series as a function of time, the system detects that the target appeared in year 1996. Poles can be seen from ascending and descending passes [49].

by the radar. It must lie on a scattering terrain, and it must be perpendicular to the ground. Poles stretching tram wires in Milan, for example, are not perfectly perpendicular, and they are not seen by the satellite.

Fig. 8 shows a car park with different scattering poles (in the aerial photo, they can be seen through their shadow). The nearby picture is a pole as seen at a ground level. The target has a very low RCS ($\widehat{\mathrm{RCS}} = 160\ \mathrm{m}^2$), and consequently, the amplitude model estimate is not reliable ($\hat{\varepsilon}_{\mathrm{fit}} = 0.69$). The AP phase, on the contrary, is reasonable ($\hat{\phi}_{\mathrm{pol}} = 3.1\ \mathrm{rad}$). As visible from the amplitude series as a function of time, the system detects that the target appeared in year 1996.

Even if the poles are quite critical due to the low scattering surface, they are very precious for connecting satellite ascending and descending passes. Such a property has been used in [49] for creating an urban digital terrain model of Milan City with tens of centimeters accuracy exploiting data acquired by ERS-1, ERS-2, and Envisat from two descending tracks (T208 and T480) and an ascending one (T487).

4) Trihedrals: The last target typology we analyze is the trihedral (about 10% in Milan). Trihedrals are usually formed by two right-angled building walls and the ground, as in a courtyard internal angle. In this case, they are included among

the scatterer typologies at ground level. Trihedrals can be rarely found at higher elevations, which are generated by appropriately arranged structural details. Trihedrals appear as pointwise in both cross-slant range and azimuth directions, but, differently from poles, they have high RCS. Furthermore, the AP phase differentiates poles and trihedrals: The second ones are characterized by a triple-bounce scattering system that rotates in the same way horizontal and vertical polarized signals do [45]. Finally, no trihedral amplitude variation as a function of temperature has been observed.

Fig. 9 is an example of a courtyard internal angle acting as a trihedral. The target has an enormous scattering surface ($\widehat{\mathrm{RCS}} = 46\,000\ \mathrm{m}^2$) and a very high phase stability ($\gamma = 0.98$). Azimuth width is detected as the theory foresees ($\hat{L}_y = 0\ \mathrm{m}$); range width is small but nonnull ($\hat{L}_x = 3\ \mathrm{m}$). However, the amplitude model fitting index is not so high as promised by the high RCS, and this suggests that many other phenomena, which are neglected in our amplitude model, can modify the received RCS. Finally, the AP phase is not so far from the trihedral theoretical behavior (AP phase $\hat{\phi}_{\mathrm{pol}} = -0.7\ \mathrm{rad}$).

Trihedrals are visible from parallel tracks as well as dihedrals, but they should be observable also under different
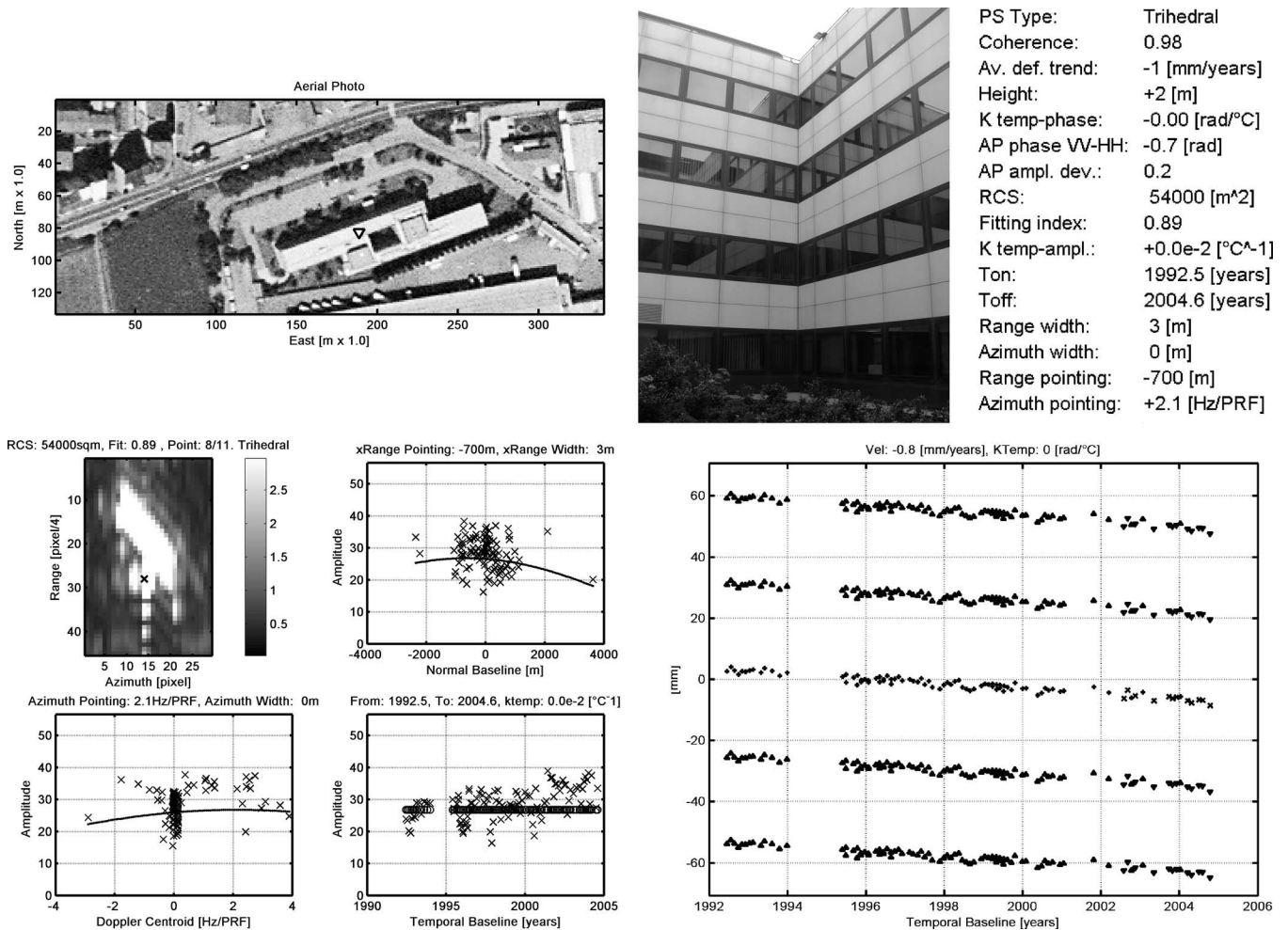
Fig. 9. Example of PS recognized as a trihedral (courtyard internal angle). The target has an enormous scattering surface ($\widehat{\text{RCS}} = 46\,000$ m^2) and a very high phase stability ($\gamma = 0.98$). Azimuth width is detected as the theory foresees ($\hat{L}_y = 0$ m); range width is small but nonnull ($\hat{L}_x = 3$ m). AP phase is not so far from the trihedral theoretical behavior (AP phase). Trihedrals can be seen under slightly different azimuth angles.

azimuth angles (e.g., in images with different DC-frequency nominal values, as passing from ERS to RADARSAT).

IV. CONCLUSION

In this paper, we tackle the problem of the physical nature of SAR PSs, providing a method for target identification and characterization by means of radar data. The three main radar measurements that have been analyzed are as follows: precise target position; target RCS as a function of the acquisition parameters; and the phase of autointerferograms generated from Envisat AP acquisitions. Amplitude data analysis, also exploiting high DCs as well as normal baseline values, was found extremely informative for the characterization of radar targets. A simple model was adopted for feature-parameter extraction. Notwithstanding its simplicity, real-data analysis confirmed the good potential of this approach for a first-order data clustering. For the first time, resonating structures have been identified through the amplitude temperature dependence. By combining all the available information, we showed the bases of an automatic algorithm for target recognition of six different target typologies (ground-level single-bounce scatterers, roof-level single-bounce scatterers, simple dihedrals, resonating

dihedrals, poles, and trihedrals). Radar data have been combined with *in situ* surveys and aerial photos, allowing a first assessment of this methodology in urban area. The physical characterization of the targets allows a better understanding of the deformation phenomena measured by the PS technique and the identification of multisensor targets that can be observed by different sensors under different acquisition geometries.

REFERENCES

[1] A. Ferretti, C. Prati, and F. Rocca, "Permanent scatterers in SAR interferometry," *IEEE Trans. Geosci. Remote Sens.*, vol. 39, no. 1, pp. 8–20, Jan. 2001.

[2] A. Ferretti, C. Prati, and F. Rocca, "Non-linear subsidence rate estimation using permanent scatterers in differential SAR interferometry," *IEEE Trans. Geosci. Remote Sens.*, vol. 38, no. 5, pp. 2202–2212, Sep. 2000.

[3] C. Colesanti, A. Ferretti, F. Novali, C. Prati, and F. Rocca, "SAR monitoring of progressive and seasonal ground deformation using the permanent

scatterers technique," *IEEE Trans. Geosci. Remote Sens.*, vol. 41, no. 7, pp. 1685–1701, Jul. 2003.

[4] V. B. H. Ketelaar and R. F. Hanssen, "Separation of different deformation regimes using PS-INSAR data," in *Proc. FRINGE*, Frascati, Italy, Dec. 1–5, 2003.

[5] D. Perissin, C. Prati, M. Engdahl, and Y. L. Desnos, "Validating the SAR wave-number shift principle with ERS–Envisat PS coherent combination," *IEEE Trans. Geosci. Remote Sens.*, vol. 44, no. 9, pp. 2343–2351, Sep. 2006.

[6] A. Ferretti, D. Perissin, C. Prati, and F. Rocca, "On the physical characterization of SAR permanent scatterers in urban areas," in *Proc. EUSAR*, Dresden, Germany, May 16–18, 2006.

[7] U. Soergel, U. Thoennessen, U. Stilla, and A. Brenner, "New opportunities and challenges for analysis of urban areas in high-resolution SAR data," in *Proc. EUSAR*, May 2004, pp. 416–418.

[8] J. H. G. Ender, "Experimental results achieved with the airborne multichannel SAR system AER-II," in *Proc. EUSAR*, May 1998, pp. 315–318.

[9] A. Moreira, R. Spielbauer, and W. Pötzsch, "Conceptual design, performance analysis and results of the high resolution real-time processor of the DLR airborne SAR system," in *Proc. IGARSS*, Pasadena, CA, 1994, pp. 912–914.

[10] J.-M. Boutry, "ONERA airborne SAR facilities," in *Proc. 2nd Int. Airborne Remote Sens. Conf.*, San Francisco, CA, Jun. 1996, pp. 1–6.

[11] J. H. G. Ender and A. R. Brenner, "PAMIR—A wideband phased array SAR/MTI system," *Proc. Inst. Electr. Eng.—Radar, Sonar, Navigation*, vol. 150, no. 3, pp. 165–172, Jun. 2003.

[12] Y. Dong, B. Forster, and C. Ticehurst, "Radar backscatter analysis for urban environments," *Int. J. Remote Sens.*, vol. 18, no. 6, pp. 1351–1364, Apr. 1997.

[13] S. Guillaso, L. Ferro-Famil, A. Reigber, and E. Pottier, "Urban area analysis based on ESPRIT/MUSIC methods using polarimetric interferometric SAR," in *Proc. Urban*, May 2003, pp. 77–81.

[14] G. Franceschetti, A. Iodice, and D. Riccio, "A canonical problem in electromagnetic backscattering from buildings," *IEEE Trans. Geosci. Remote Sens.*, vol. 40, no. 8, pp. 1787–1801, Aug. 2002.

[15] U. Soergel, U. Thoennessen, and U. Stilla, "Reconstruction of buildings from interferometric SAR data of built-up areas," in *Proc. PIA, IAPRS*, 2003, vol. 34, pp. 59–64. Part 3/W8.

[16] M. Shinozuka, R. Ghanem, B. Houshmand, and B. Mansuri, "Damage detection in urban areas by SAR imagery," *J. Eng. Mech.*, vol. 126, no. 7, pp. 769–777, Jul. 2000.

[17] U. Stilla, E. Michaelsen, and U. Soergel, "Perceptual grouping of regular structures for automatic detection of man-made objects—Examples from IR and SAR," in *Proc. IGARSS*, Jul. 2003, pp. 3525–3527.

[18] R. Bolter, "Reconstruction of man-made objects from high resolution SAR images," in *Proc. IEEE Aerosp. Conf.*, Mar. 2000, vol. 3, pp. 287–292.

[19] P. Gamba, B. Houshmand, and M. Saccani, "Detection and extraction of buildings from interferometric SAR data," *IEEE Trans. Geosci. Remote Sens.*, vol. 38, no. 1, pp. 611–617, Jan. 2000.

[20] M. Quartulli and M. Dactu, "Bayesian model based city reconstruction from high resolution ISAR data," in *Proc. IEEE/ISPRS Joint Workshop Remote Sens. Data Urban Areas*, Rome, Italy, Nov. 2001, pp. 58–63.

[21] U. Soergel, K. Schuls, U. Thonnessen, and U. Stilla, "3D visualization of interferometric SAR data," in *Proc. EUSAR*, May 2000, pp. 305–308.

[22] C. Tison, F. Tupin, and H. Maitre, "Extraction of urban elevation models from high resolution interferometric SAR images," in *Proc. EUSAR*, May 2004, pp. 411–414.

[23] S. Guillaso, L. Ferro-Famil, A. Reigber, and E. Pottier, "Building characterization using L-band polarimetric interferometric SAR data," *IEEE Geosci. Remote Sens. Lett.*, vol. 2, no. 3, pp. 347–351, Jul. 2005.

[24] J. S. Lee, I. Jurkevich, P. Dewaele, P. Wambacq, and A. Oosterlinck, "Speckle filtering of synthetic aperture radar images: A review," *Remote Sens. Rev.*, vol. 8, no. 3, pp. 313–340, 1994.

[25] R. Touzi, "A review of speckle filtering in the context of estimation theory," *IEEE Trans. Geosci. Remote Sens.*, vol. 40, no. 11, pp. 2392–2404, Nov. 2002.

[26] J.-C. Souyris, C. Henry, and F. Adragna, "On the use of complex SAR image spectral analysis for target detection: Assessment of polarimetry," *IEEE Trans. Geosci. Remote Sens.*, vol. 41, pt. 1, no. 12, pp. 2725–2734, Dec. 2003.

[27] A. Lopes, J. Bruniquel, F. Sery, J. C. Souyris, and F. Adragna, "Optimal target detection using one channel SAR complex imagery: Application to ship detection," in *Proc. IGARSS*, Jul. 1998, pp. 813–815.

[28] V. Larson, L. Novak, and C. Stewart, "Joint spatial-polarimetric whitening filter to improve SAR target detection performance for spatially distributed targets," *Proc. SPIE*, vol. 2230, pp. 285–301, Jun. 1994.

[29] A. Arnaud, "Ship detection by SAR interferometry," in *Proc. IGARSS*, Jul. 1999, pp. 2616–2618.

[30] R. Z. Schneider, K. Papathanassiou, I. Hajnsek, and A. Moreira, "Polarimetric interferometry over urban areas: Information extraction using coherent scatterers," *IEEE Trans. Geosci. Remote Sens.*, vol. 44, no. 4, pp. 971–984, Apr. 2006.

[31] F. T. Ulaby, R. K. Moore, and A. K. Fung, *Microwave Remote Sensing*. Reading, MA: Addison-Wesley, 1982.

[32] F. Caltagirone, G. Manoni, P. Spera, and R. Vigliotti, "SkyMed/COSMO mission overview," in *Proc. IGARSS*, Jul. 1998, pp. 683–685.

[33] R. W. Zahn and E. H. Velten, "Enabling technologies for the TerraSAR mission," in *Proc. IGARSS*, Honolulu, HI, Jul. 2000, vol. 3, pp. 1174–1176.

[34] F. Dell'Acqua and P. Gamba, "Texture-based characterization of urban environments on satellite SAR images," *IEEE Trans. Geosci. Remote Sens.*, vol. 41, no. 1, pp. 153–159, Jan. 2003.

[35] F. Dell'Acqua and P. Gamba, "Detection of urban structures in SAR images by robust fuzzy clustering algorithms: The example of street tracking," *IEEE Trans. Geosci. Remote Sens.*, vol. 39, no. 10, pp. 2287–2297, Oct. 2001.

[36] F. Dell'Acqua, P. Gamba, and G. Lisini, "Improvements to urban area characterization using multitemporal and multiangle SAR images," *IEEE Trans. Geosci. Remote Sens.*, vol. 41, pt. 1, no. 9, pp. 1996–2004, Sep. 2003.

[37] A. Arnaud, N. Adam, R. Hanssen, J. Inglada, J. Duro, J. Closa, and M. Eineder, "ASAR ERS interferometric phase continuity," in *Proc. IGARSS*, Jul. 21–25, 2003, vol. 2, pp. 1133–1135.

[38] A. Monti Guarneri and C. Prati, "ERS–ENVISAT combination for interferometry and super-resolution," in *Proc. ERS-ENVISAT Symp.*, Gothenburg, Sweden, 2000.

[39] J. Closa, N. Adam, A. Arnaud, J. Duro, and J. Inglada, "High resolution differential interferometry using time series of ERS and ENVISAT SAR data," in *Proc. FRINGE Symp.*, Dec. 1–5, 2003.

[40] J. Closa, J. Duro, J. Inglada, and A. Arnaud, "Combination of ERS and multiple modes of ENVISAT SAR data for differential interferometric applications," in *Proc. ENVISAT Symp.*, Salzburg, Austria, Sep. 6–10, 2004.

[41] R. Bamler, "Interferometric stereo radargrammetry—Absolute height determination from ERS–ENVISAT interferograms," in *Proc. IGARSS*, Jul. 2000, pp. 742–745.

[42] C. Colesanti, A. Ferretti, D. Perissin, C. Prati, and F. Rocca, "ERS–Envisat permanent scatterers interferometry," in *Proc. IGARSS*, 2003, vol. 2, pp. 1130–1132.

[43] P. Marinkovic, G. Ketelaar, and R. Hanssen, "A controlled Envisat/ERS permanent scatterer experiment, implications of corner reflector monitoring," in *Proc. CEOS SAR Workshop*, Ulm, Germany, May 27–28, 2004.

[44] U. Wegmüller, C. Werner, T. Strozzi, and A. Wiesmann, "ERS–ASAR integration in the interferometric point target analysis," in *Proc. FRINGE*, Frascati, Italy, Nov. 28–Dec. 2 2005.

[45] J. Inglada, C. Henry, and J.-C. Souyris, "Assessment of ASAR/IMS multi-polarization images phase difference in the framework of persistent scatterers interferometry," in *Proc. ENVISAT Congr.*, Salzburg, Austria, Sep. 20–24, 2004.

[46] J. Inglada, J. C. Souyris, and C. Henry, "Incoherent SAR polarimetric analysis over point targets," *IEEE Geosci. Remote Sens. Lett.*, vol. 3, no. 2, pp. 246–249, Apr. 2006.

[47] A. Tarantola, *Inverse Problem Theory*. Amsterdam, The Netherlands: Elsevier, 1987.

[48] *SAR Geocoding: Data and Systems*, G. Schreier, Ed. Karlsruhe, Germany: Wichmann, 1993.

[49] D. Perissin and F. Rocca, "High-accuracy urban DEM using permanent scatterers," *IEEE Trans. Geosci. Remote Sens.*, vol. 44, no. 11, pp. 3338–3347, Nov. 2006.

[50] A. Monti Guarneri, C. Cafforio, P. Guccione, P. Pasquali, and Y. L. Desnos, "ENVISAT ASAR scanSAR interferometry," in *Proc. IGARSS*, Jul. 21–25, 2003, vol. 2, pp. 1124–1126.

[51] P. J. Van Zyl, "Unsupervised classification of scattering behaviour using radar polarimetry data," *IEEE Trans. Geosci. Remote Sens.*, vol. 27, no. 1, pp. 36–45, Jan. 1989.

[52] A. L. Gray, P. W. Vachon, C. E. Livingstone, and T. I. Lukowski, "Synthetic aperture radar calibration using reference reflectors," *IEEE Trans. Geosci. Remote Sens.*, vol. 28, no. 3, pp. 374–383, May 1990.

[53] G. Ruck, D. Barrick *et al. Radar Cross Section Handbook*. New York: Plenum, 1970.

[54] F. Gatelli *et al.*, "The wavenumber shift in SAR interferometry," *IEEE Trans. Geosci. Remote Sens.*, vol. 32, no. 4, pp. 855–865, Jul. 1994.

[55] A. Ferretti, C. Colesanti, D. Perissin, C. Prati, and F. Rocca, "Effect of evaluating the effect of the observation time on the distribution of SAR permanent scatterers," in *Proc. FRINGE*, Frascati, Italy, Dec. 2003.

[56] *Genetic Algorithms and Simulated Annealing*, L. Davis, Ed. London, U.K.: Pitman, 1987.

Alessandro Ferretti was born in Milan, Italy, on January 27, 1968. After his classical studies during high school, he received the laurea degree in electrical engineering (*cum laude*) from Politecnico di Milano (POLIMI), Milan, Italy, in 1993, the M.S. degree in information technology (*cum laude*) from the Center of Excellence for Research, Innovation, Education, and Industrial Labs., working on digital signal processing, and the Ph.D. degree in electrical engineering from POLIMI.

In May 1994, he joined the POLIMI radar group, working on SAR interferometry and digital elevation model reconstruction. After devoting most of his research efforts on multitemporal SAR data stacks, he developed, together with Prof. Rocca and Prof. Prati, what is now called the "PS technique," a technology patented in 1999, which can overcome most of the difficulties encountered in conventional SAR interferometry. In March 2000, he founded, together with Prof. Rocca, Prof. Prati, and POLIMI, the company "Tele-Rilevamento Europa," where he is currently the Managing Director. He has been involved in many projects financed by the European Space Agency and was the promoter, in 2003, of the first interferometric archive of RADARSAT data on a national level. His research interests include radar data processing, optimization algorithms, differential interferometry, and use of remote sensing information for civil-protection applications.

Daniele Perissin was born in Milan, Italy, in 1977. He received the M.S. degree in telecommunications engineering and the Ph.D. degree in information technology from Politecnico di Milano, Milan, Italy, in 2002 and 2006, respectively.

He joined the research group of Prof. F. Rocca and Prof. C. Prati at Politecnico di Milano in 2002, and since then, he has been working on the permanent scatterer technique. He holds a patent on the use of urban dihedral reflectors for combining multisensor synthetic aperture radar data, which is his main interest.